Research Article

Hazards and Treatment of Collapsible Loess Foundation on Ultrahigh Voltage Transmission Lines

Longfei Zhang [ID],[1] **Zaiqiang Hu** [ID],[1] **Hongru Li** [ID],[1] **Haicheng She** [ID],[2] **Xiaoliang Wang** [ID],[1] **Xiaoning Han** [ID],[1] **and Xi Yang** [ID][1]

[1]*Institute of Geotechnical Engineering, Xi'an University of Technology, Xi'an 710048, China*
[2]*School of Urban Construction, Yangtze University, Jingzhou 434032, China*

Correspondence should be addressed to Zaiqiang Hu; huzq@xaut.edu.cn

With the development of ultrahigh voltage transmission line construction in northwest China, an increasing number of overhead transmission lines are crossing the loess regions. Ensuring the stability of electricity transmission towers and mitigating the risk of collapse are crucial prerequisites for the construction of transmission lines. Taking the 750 kV demonstration electricity transmission line in Guanting–Lanzhou East as an example, representative loess samples were selected for compression and collapsing sensitivity tests. Four foundation treatment schemes were designed, and the wetting deformation characteristics were investigated through numerical simulation of the rainfall infiltration process. Corresponding optimisation schemes were proposed. The collapsing process was divided into four stages through laboratory collapsing tests. The relationship function between saturation and the Duncan–Chang model parameters of loess was established, which was introduced into the finite element model to consider the rainfall infiltration process. The analysis of the displacement field, and loess saturation field with time after rainfall infiltration for the four schemes showed that adding a lime-stabilised soil cushion layer and waterproof layer to the inclined column foundation had the best effect. Given that the design scheme needs to consider safety and economy, the thickness of the cushion layer was optimised, thereby reducing the use of lime-stabilised soil by 20%. Research findings provide meaningful guidance for the design of transmission tower foundations in loess areas.

1. Introduction

With the comprehensive advancement of the construction project of the 750 kV transmission backbone network in northwest China, many problems have emerged in the design and construction stages, making it urgent to conduct in-depth research on the effects of collapsible geological conditions on the foundation to ensure the successful construction and stable operation of the electricity transmission line. As the first 750 kV transmission line in northwest China, the Guanting–Lanzhou East electricity transmission line has a total length of 146 km and is a crucial supporting project for the Gongboxia hydropower station. Figure 1 shows that the loess along the transmission line is mainly silty loess, with a large natural porosity and a tendency to collapse when encountering water [1–3]. As shown in (Figure 1(a)), its

latitude range is 35°42′ N–36°00′ N and its longitude range is 102°36′ E–24°12′ E.

To economically and safely address the collapse sensitivity of loess when encountering water, various methods can be employed for foundation treatment. The goal is to eliminate collapse, increase bearing capacity, and ensure the stability of structures [4, 5]. Traditionally, lime-stabilised soil cushion layers have been used to enhance the bearing capacity of loess foundations, but they may result in significant settlement if there is a weak soil layer underneath [6–8]. Alternatively, a gravel cushion layer consisting of well-graded gravel, pebbles, and sand can be used in areas with high groundwater levels [9, 10]. Dynamic compaction is an economical method that disrupts the soil structure and forms a compacted layer, although its effectiveness decreases with depth [11–13]. Other methods include compacted piles of lime-stabilised soil [14–16], vibro-replacement stone piles [17–19],

FIGURE 1: (a) Guanting–Lanzhou East electricity transmission line, (b) Guanting substation, (c) transmission tower, and (d) Hongliangying substation.

reinforced concrete precast piles [20–22], cast-in-place piles [23, 24], and cement mixing piles [25–27]. These methods offer varying benefits such as increased bearing capacity, improved stability, and cost efficiency. However, each method has its own considerations, such as noise during construction or potential pollution on-site. Overall, selecting the appropriate foundation treatment method depends on factors such as the type of collapsibility, soil conditions, project scale, and economic and safety requirements.

In the case of transmission tower foundation, the main reason for foundation settlement is water immersion, which causes rapid destruction of the loess structure. The key to dealing with collapsible sensitivity in loess is to ensure that the foundation is not exposed to water [28]. In view of the tower type, terrain, geology, collapsibility level, and groundwater level, appropriate foundation treatment may be necessary when waterproofing cannot sufficiently meet the requirements for severe cases of waterlogging. Accounting for the special characteristics of electricity transmission line engineering and project experience, the commonly used method for foundation treatment is the lime-stabilised soil cushion layer. This method uses manual labour, requires no special equipment, is suitable for various terrain conditions, and has good effects on all levels of collapsible sensitivity in loess [29, 30]. Thus, how can the size of the lime-stabilised

soil cushion layer be determined for large transmission tower foundations on loess? This problem requires understanding of the collapsible deformation mechanism of loess and establishing corresponding predictive deformation models. The essence of collapsible deformation is a special type of plastic deformation, characterised by suddenness, discontinuity, and irreversibility [31]. To more accurately reflect the deformation characteristics of unsaturated soil, many scholars have established constitutive models for unsaturated soil within the framework of nonlinear elastic [31] or elastoplastic theory [32, 33]. These models can reflect the deformation of unsaturated loess caused by changes in stress state but cannot account for the effect of the infiltration process. Centrifugal model tests [34, 35] and on-site water immersion tests [36, 37] can provide accurate results for the water infiltration process and development of collapsing deformation of loess foundations; however, these methods require a long time and relatively high costs. The Duncan–Chang model considers the nonlinear and time-dependent nature of soil response by incorporating hyperbolic equations. It can accurately capture the stress–strain relationships, including the initial elastic behaviour, yielding, and subsequent plastic deformations. This model has proven to be effective in simulating soil behaviour in different engineering applications, such as slope stability analysis, foundation design, and

FIGURE 2: Basic physical and mechanical parameters test of loess: (a) iron tower foundation; (b) loess; (c) specific gravity test; (d) particle analysis test; (e) permeability test; (f) liquid plastic limit test.

soil-structure interaction [38]. However, the Duncan–Chang model cannot reflect the influence of changes in soil moisture content.

This article analysed the characteristics of collapsible loess, the situation of collapsible loess sites along the northwest 750 kV transmission project route, conventional treatment techniques for collapsible loess, and treatment techniques and effects used in transmission line projects. Using the demonstration electricity transmission line project in Guanting–Lanzhou East as an example, indoor experiments were conducted on the loess at the project site. On-site soil samples and treatments were experimentally studied and analysed using a self-developed program for finite element analysis. In addition, data from operating transmission lines were investigated to provide a basis for the design and construction of high-voltage tower foundations.

2. Test Soil and Main Physical Parameters

The tested loess were taken from the foundation pits of a transmission tower in Nantang Village, Liujiaxia, Gansu Province, as shown in Figure 2. The soil was collected at depths of 2 and 4 m below the current ground level, with a brownish-yellow colour, relatively large pores, well-developed wormholes, and low water content. At the soil collection site, the soil samples were made into cubes with side lengths of 20–30 cm, marked with the top and bottom orientations, wrapped in plastic wrap, and carefully transported to the laboratory for testing. Disturbance during soil collection and transportation was minimised as much as possible.

On the basis of the results of specific gravity tests, particle size analyses, permeability tests, and liquid limit tests, the main physical parameters of the loess at depths of 2 and 4 m are shown in Table 1. The samples had similar water contents, but the loess at 2 m had a higher silt particle content and smaller void ratio and permeability coefficient, whereas the loess at 4 m had a larger void ratio. According to the classification suggestion for loess types [39], both tested samples belong to silty loess, mechanical properties of which are greatly affected by changes in water content.

3. Compression Test

The compression test can reflect the compression characteristics and obtain the compression modulus of soil under different pressure ranges. To study the deformation and strength characteristics of undisturbed loess, 12 sets of samples with different water contents were selected for compression tests in this section.

TABLE 1: Physical and mineralogical characterisation of the tested loess.

Property	Value at 2 m	Value at 4 m
Specific gravity	2.68	2.70
Natural water content w (%)	11.2	10.8
Natural density (g/cm^3)	1.50	1.45
Void ratio	0.99	1.05
Atterberg limits		
Liquid limit (%)	27.22	28.87
Plastic limit (%)	17.08	18.51
Plasticity index (%)	10.13	10.36
Particle size distribution (%)		
Sand >0.075 mm	27	37
Silt 0.075–0.005 mm	64	55.5
Clay <0.005 mm	7	7.5
Permeability characteristics		
Horizontal permeability coefficient (10^{-5} cm/s)	1.0	13.2
Vertical permeability coefficient (10^{-5} cm/s)	3.0	9.3
Collapsibility characteristics		
Coefficient of collapsibility	0.027	0.032
Coefficient of self-weight collapsibility	0.008	0.023

3.1. Test Scheme. About 12 sets of samples were prepared by controlling the water content of samples through dehydration (natural drying method) and humidification (water film transfer method). The water content of undisturbed loess at 2 m is 7%, 11.2% (natural water content), 15%, 19%, 23%, and 36.8% (saturation water content); and the water content of undisturbed loess at 4 m is 7%, 10.8% (natural water content), 15%, 19%, 23%, and 39% (saturation water content). The prepared samples were placed in a moisturising device for more than 48 hr to ensure a uniform diffusion of moisture in the samples.

The lever-controlled consolidation instrument was used in the test. After the moisture of the samples was uniform, vertical loads were applied to the samples with different water contents in the order of 50, 100, 200, and 400 kPa. At each pressure level, when the deformation of the sample was stable (the deformation was less than 0.01 mm/hr), the stress and deformation of the soil sample were recorded. The method of multiple parallel samples in each group was used to reduce the adverse effect of soil randomness.

3.2. Test Result. Figures 3 and 4 show that the previous e–lg p curve is relatively flat at the same water content, with an obvious inflection point. Before this point, the stress in the soil did not reach the structural strength, and only partial connection points were broken or moved, resulting in only a small amount of deformation and a slight decrease in porosity. After the stress in the soil exceeded the structural strength, the framework of the interparticle void structure was damaged. As the particles rapidly slid into the cavities of the interparticle voids, the deformation of the soil rapidly increased and the porosity decreased rapidly.
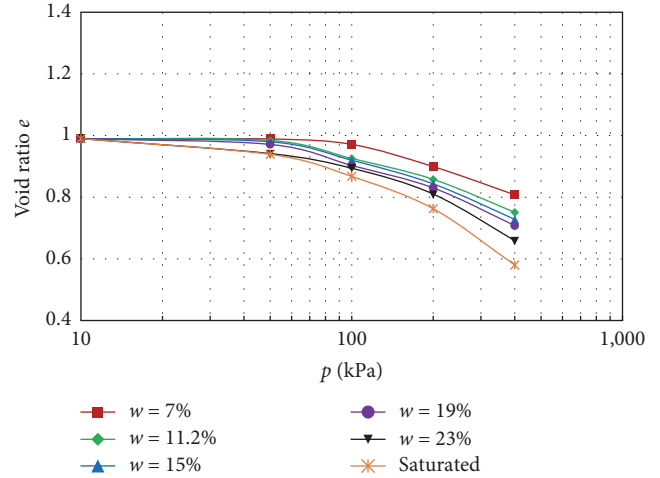
FIGURE 3: e–lg p curves with different water contents at 2 m.
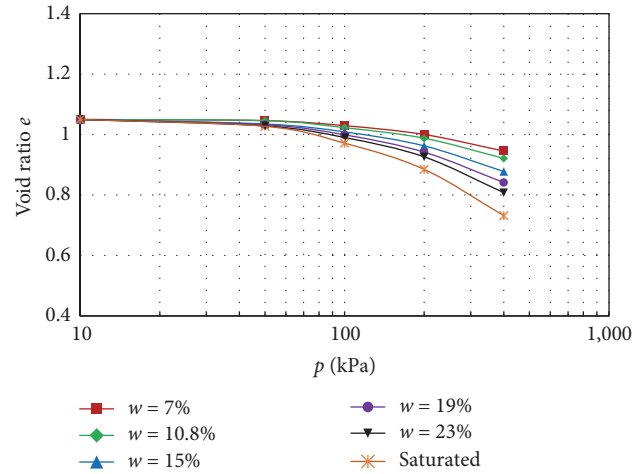
FIGURE 4: e–lg p curves with different water contents at 4 m.

The comparison of the e–lg p curves at different water contents indicated that the structural strength of the undisturbed loess decreases rapidly with the increase of water content, and the decrease in strength at low water content is considerably greater than at a high water content. As the initial water content increases, the difference between the e–lg p curves gradually becomes smaller, indicating that the collapsibility decreases with the increase of initial water content, and the compressibility increases with humidification.

The compression modulus is the ratio of the sample's vertical additional stress and vertical strain. The smaller the compression modulus E_s is, the easier the soil will be compressed. The analysis of the relationship curves between the compression modulus and the saturation at different pressure intervals in Figures 5 and 6 implied that the compression modulus obtained from the samples at the saturation water content state is slightly smaller than that at the natural water content state, but the deviation is small and the data are reasonable. At the same saturation, the compression modulus increases with pressure. Within the same pressure interval, the compression modulus decreases with the increase
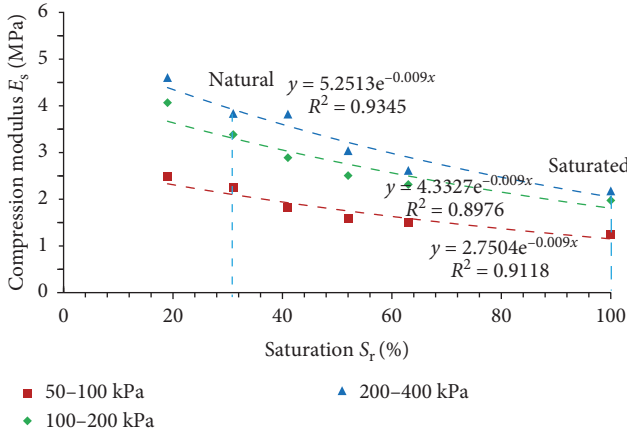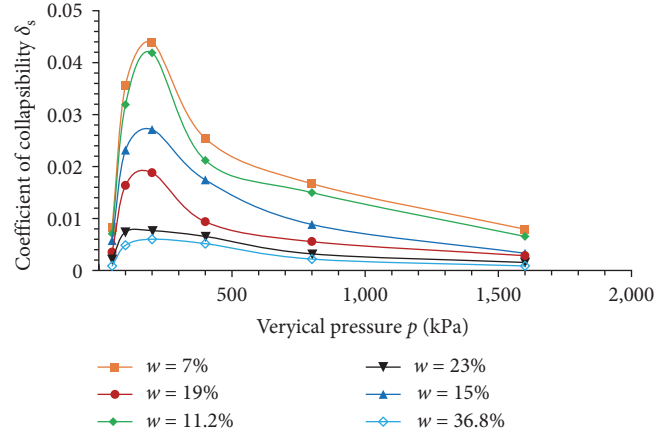
FIGURE 5: E_s–S_r curves of loess at a depth of 2 m.

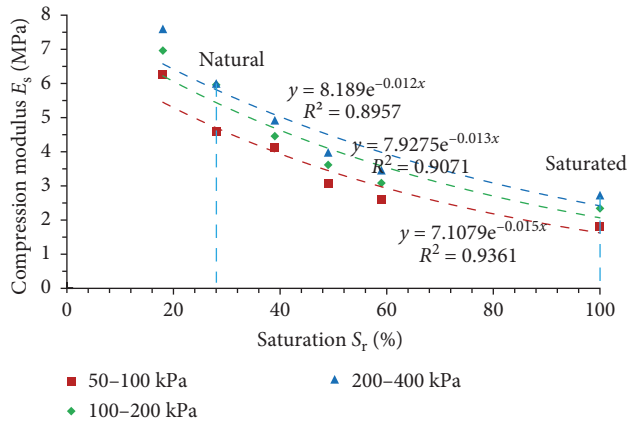FIGURE 7: δ_s–p curves of loess at a depth of 2 m.
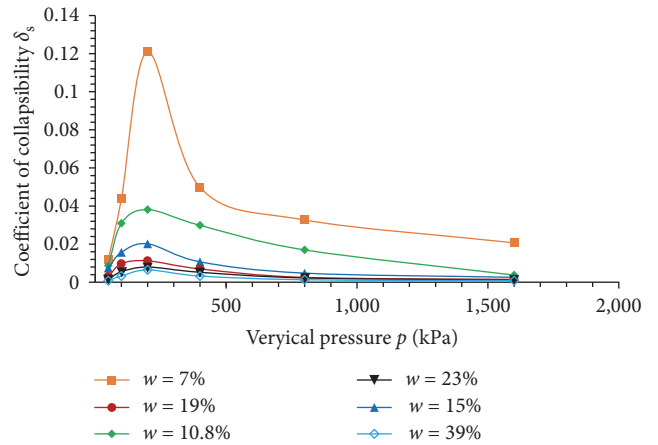

FIGURE 6: E_s–S_r curves of loess at a depth of 4 m.

FIGURE 8: δ_s–p curves of loess at a depth of 4 m.

TABLE 2: E–v model parameters of loess with different water contents.

Loess state Depths of loess	Water content	K (kPa)	n	R_f	c (kPa)	φ (°)	G	F	D
2 m	11.2% (natural)	104.41	0.43	0.77	48	28.96	0.20	0.10	3.52
	15%	74.56	0.60	0.74	42	26.41	0.22	0.09	2.55
	19%	66.29	0.60	0.71	35	25.41	0.25	0.11	3.04
	23%	65.32	0.63	0.73	30	24.23	0.26	0.11	3.06
	36.8% (saturated)	52.39	0.64	0.71	34	23.91	0.28	0.10	2.57
4 m	10.8% (natural)	153.61	0.32	0.82	55	29.18	0.17	0.09	3.48
	15%	143.95	0.33	0.87	48	28.96	0.20	0.09	3.81
	19%	110.51	0.39	0.84	41	28.00	0.21	0.09	3.59
	23%	76.06	0.53	0.83	33	27.09	0.24	0.10	3.98
	39% (saturated)	46.33	0.82	0.70	25	25.00	0.26	0.09	4.23

in saturation, which can be fitted using an exponential function. The comparison of the compression modulus changes at different depths shows that the compression modulus of loess varies greatly at a low water content but is almost identical at the saturation state. Overall, the relationship between saturation and compression modulus can be described using an exponential function.

4. Loess Collapse Test

When loess is subjected to water immersion under a certain pressure, the structure will rapidly deteriorate, and significant additional settlement will occur. As a foundation for tower bases, its settlement is closely related to engineering safety and directly affects the design of foundation treatment.
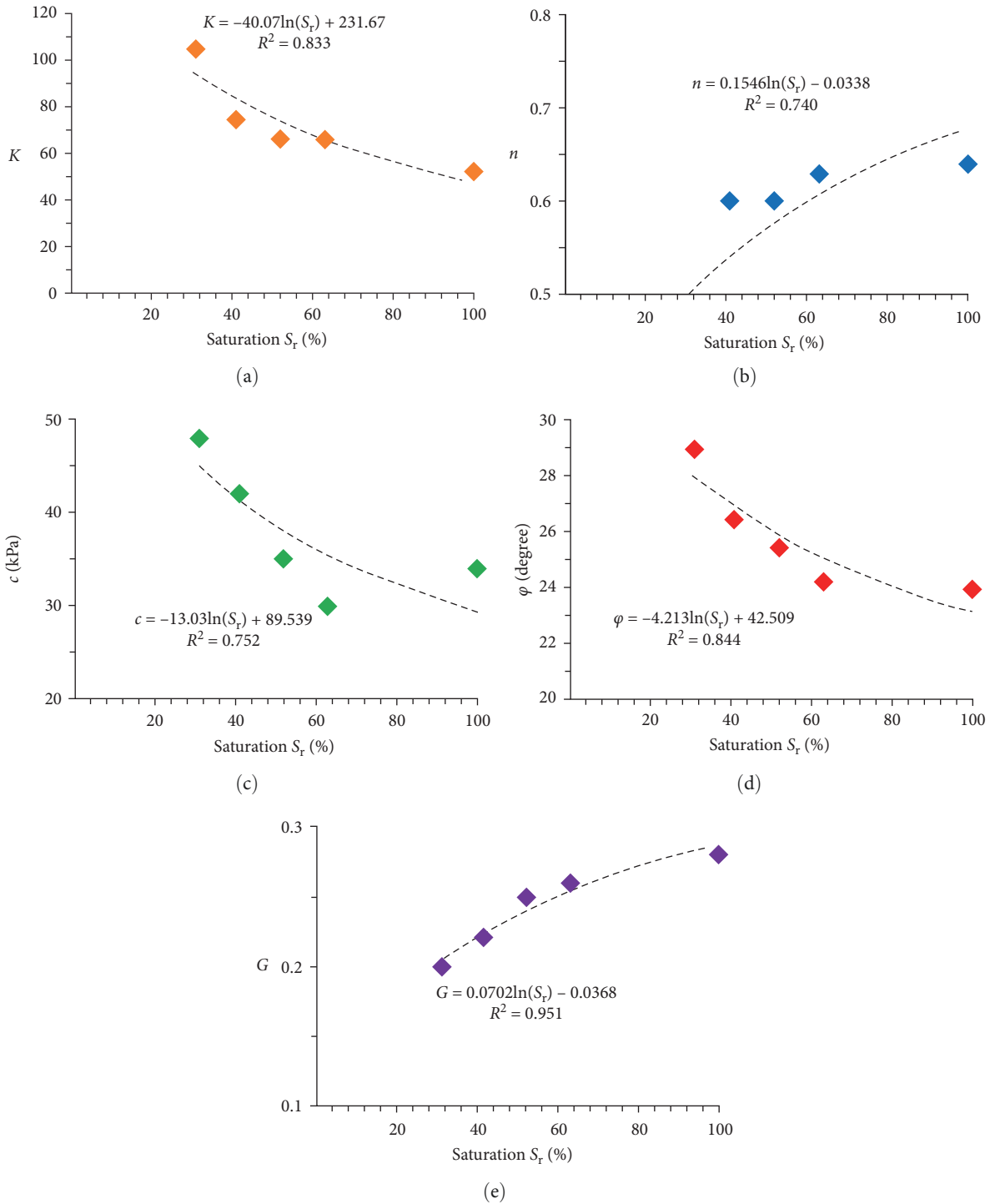
$$K = -40.07\ln(S_r) + 231.67$$
$$R^2 = 0.833$$

(a)

$$n = 0.1546\ln(S_r) - 0.0338$$
$$R^2 = 0.740$$

(b)

$$c = -13.03\ln(S_r) + 89.539$$
$$R^2 = 0.752$$

(c)

$$\varphi = -4.213\ln(S_r) + 42.509$$
$$R^2 = 0.844$$

(d)

$$G = 0.0702\ln(S_r) - 0.0368$$
$$R^2 = 0.951$$

(e)

FIGURE 9: Change law of parameters with saturation at a depth of 2 m. Fitted curve for (a) material constant K, (b) material constant n, (c) cohesion c, (d) internal friction angle φ, and (e) material constant G.

The test of the collapsing properties of loess is an important test item.

4.1. Test Scheme. The soil samples used in the test are the same as those used in the previous compression test. First, different water content samples were gradually loaded with vertical pressures of 50, 100, 200, 400, 800, and 1,600 kPa. After the first level of pressure was applied, the deformation

readings were measured every hour until the sample deformation became stable, and the second level of pressure was then applied, and so on. After the sample deformation became stable under the specified pressure, pure water was injected into the container until the water level was above the top of the sample, and the deformation readings were measured every hour until the sample deformation became stable (with a deformation rate of less than 0.01 mm/hr). The
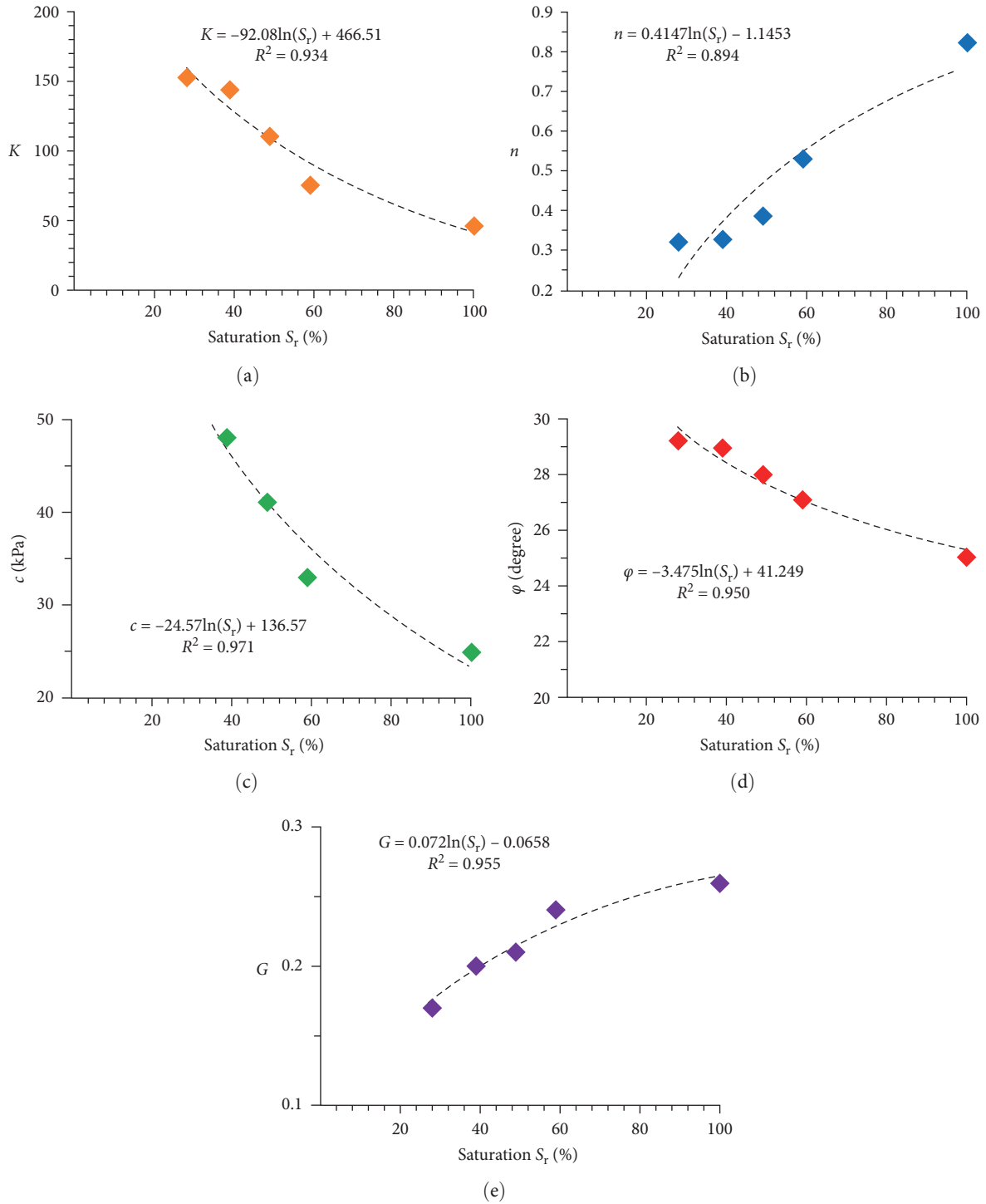
Figure 10: Change law of parameters with saturation at a depth of 4 m. Fitted curve for (a) material constant K, (b) material constant n, (c) cohesion c, (d) internal friction angle φ, and (e) material constant G.

collapsibility coefficient δ_{wp} and the self-weight collapsibility coefficient δ_{zs} were calculated using Equations (1) and (2). When determining the self-weight collapsibility coefficient, the overlying soil saturation was set to 85%, and the saturated self-weight pressures of the overlying soil at 2 and 4 m were determined to be 34.74 and 68.69 kPa, respectively. The self-weight collapsing deformation was measured by loading the

sample to the saturated self-weight soil pressure of the overlying soil.

$$\delta_{wp} = \frac{h_p - h_p'}{h}, \tag{1}$$

where h_p is the height of the sample after stable deformation at a certain pressure level, h_p' is the height of the sample after
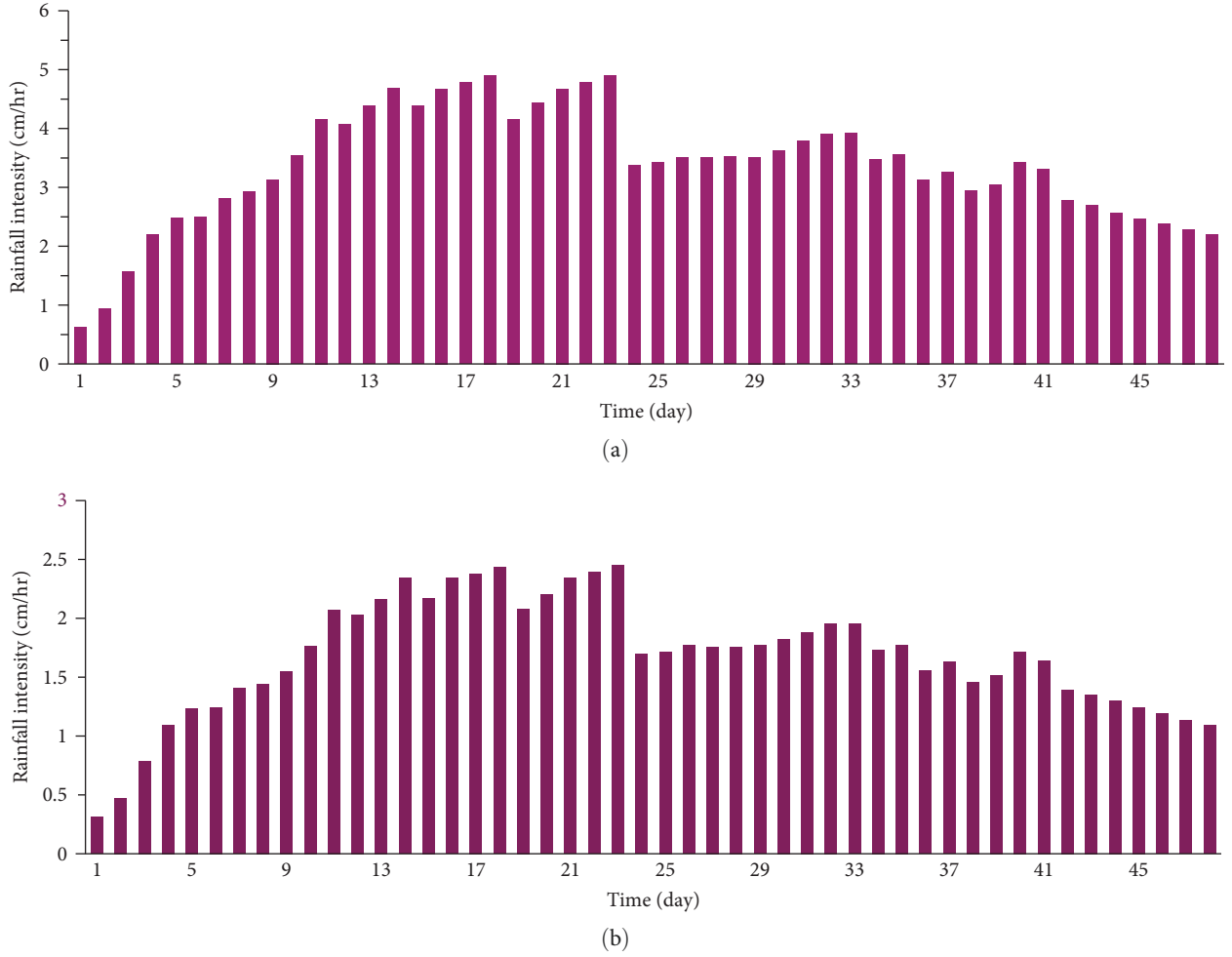
(a)

(b)

FIGURE 11: Rainfall infiltration intensity map: (a) schemes 1 and 2; (b) schemes 3 and 4.

stable deformation due to immersion in water at a certain pressure level, and h is the initial height of the sample.

$$\delta_{zs} = \frac{h_z - h_z^{'}}{h}, \tag{2}$$

where h_z is the height of the sample after stable deformation under saturated self-weight pressure and $h_z^{'}$ is the height of the sample after stable deformation due to immersion and collapse under saturated self-weight pressure.

4.2. Test Result. Figures 7 and 8 show the relationship curves between the collapsibility coefficient and pressure for soil samples at different depths. The collapsibility coefficient is the highest at a vertical pressure of 200 kPa and then gradually decreases until the curves tend to convergence. Under the conditions of natural water content and vertical pressure as the overlying self-weight load, the collapsibility coefficient of loess at 2 m is 0.027, which belongs to mildly collapsible loess, and that at 4 m is 0.039, which belongs to moderately collapsible loess.

Under the same vertical pressure, the collapsibility coefficient is more sensitive to changes in water content when the

initial water content is lower, whereas its sensitivity to changes in water content decreases when the initial water content is higher. Given the relatively large pores and low dry density, the collapsibility coefficient of the loess at 4 m is considerably higher than that at 2 m under low water content conditions, whereas they are more similar under high water content conditions.

Under the same water content conditions, the δ_s–p curve can be divided into four stages. In the additional compression deformation stage, the compression curve demonstrates an approximately linear behaviour, which can be attributed to the compression of pores and microstructural adjustments within the soil. During the collapsing initiation stage, as the pressure increases, the compression curve transitions into nonlinear characteristics. This phenomenon occurs due to further microstructural adjustments and rearrangement of the soil, resulting in an increased number of particle contacts and reorientation. In the collapsing development stage, within higher pressure ranges, the compression curve exhibits a steeper decline. This behaviour arises from the continuous increase in particle contacts and the attainment of a relatively dense microstructure. Finally, in the collapsing attenuation stage,
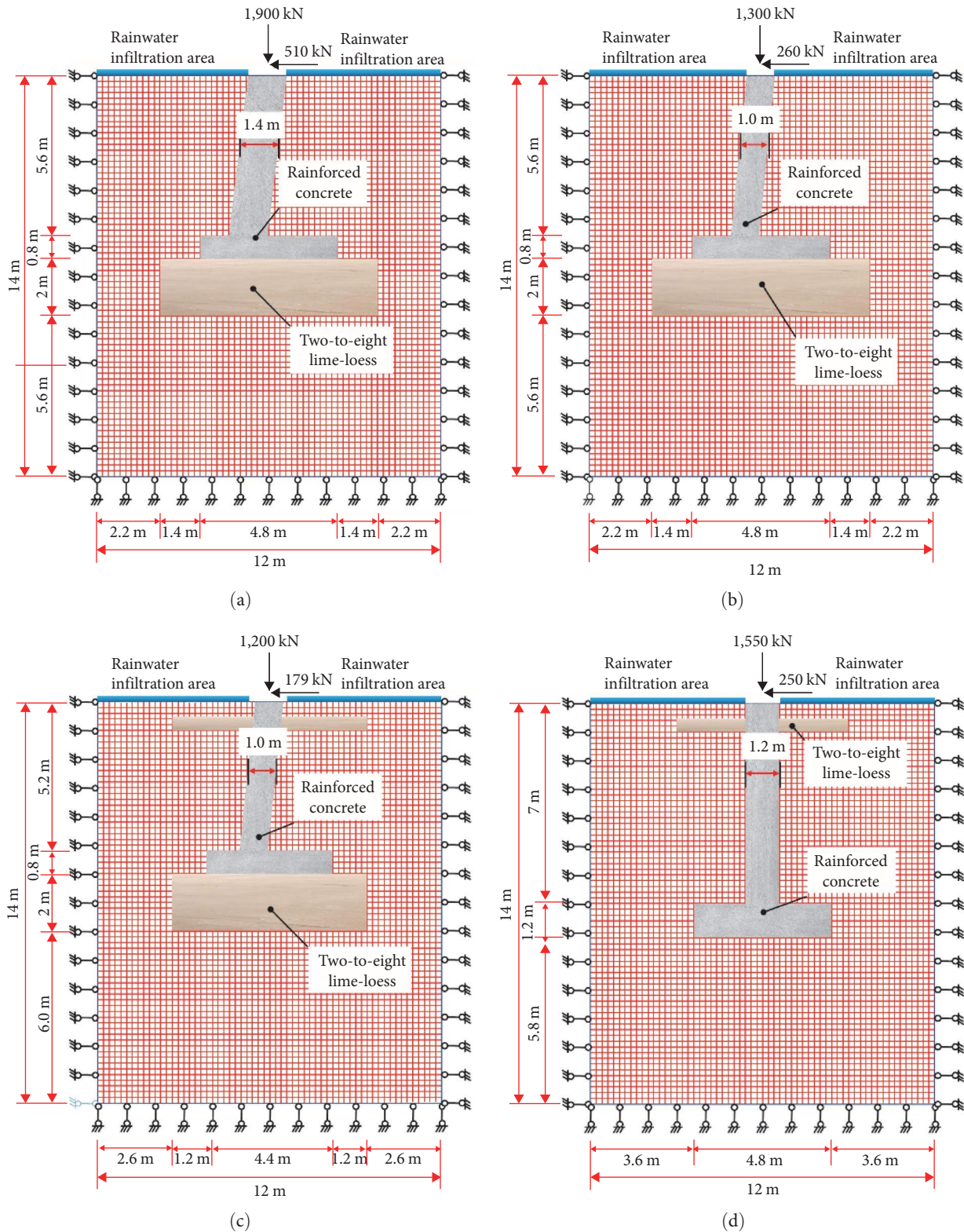
FIGURE 12: Schematic of calculation model: (a) scheme 1; (b) scheme 2; (c) scheme 3; (d) scheme 4.

the compression curve tends to flatten. This occurs because the soil particles have reached a state of near-full compaction, limiting further compaction. These stages correspond to the process of destruction and reorganisation of the microscopic structure of the soil and are closely related to its evolution [40, 41].
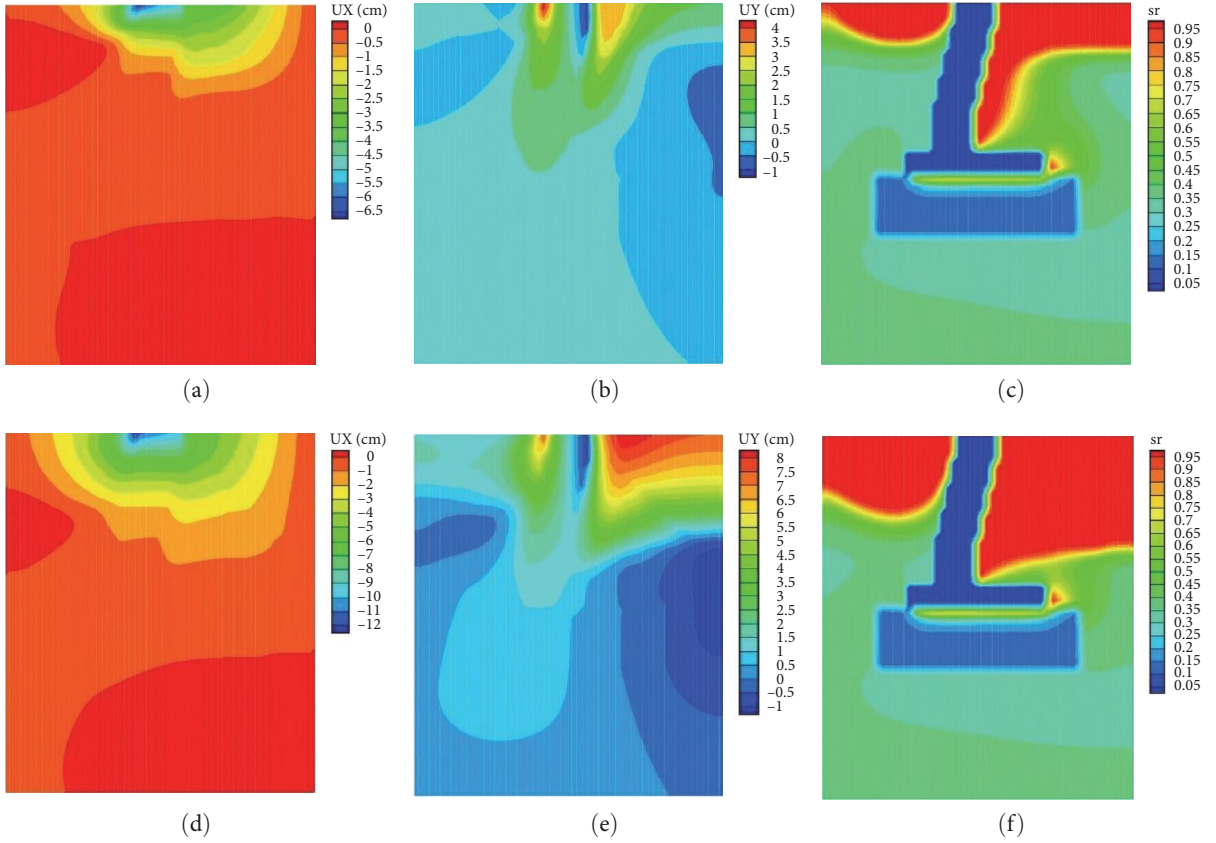
FIGURE 13: Scheme 1: (a)–(c) Horizontal displacement (UX), vertical displacement (UY), and saturation (sr) after 30 hr of rainfall infiltration; (d)–(f) the horizontal displacement (UX), vertical displacement (UY), and saturation (sr) after rainfall infiltration ceases.

5. Simulation of Foundation Settlement

5.1. Engineering Problems. The demonstration transmission line in Guanting–Lanzhou East is China's first 750 kV transmission line project, which stretches around 146 km from the Guanting substation in Minhe County, Qinghai Province, to the Hongliangying substation in the east of Lanzhou, Gansu Province. The line mainly runs in an east–west direction, roughly passing through Minhe County in Qinghai Province and Yongjing County, Dongxiang Autonomous County, Lintao County, and Yuzhong County in Gansu Province. These areas are located in the Longxi region, where the collapsibility of loess is most severe in China, with a heavy thickness of loess and various topographic forms.

Given the particularity of the electricity transmission line, construction methods, such as dynamic compaction and cast-in-place pile, have complex construction procedures, making it difficult to maintain quality control. The comprehensive cost required during the construction period is also considerable. Moreover, in actual engineering projects, hands-on experience implementing these techniques is limited. Therefore, the handling of foundation pits in some electricity transmission line projects mainly relies on the use of a lime-stabilised soil cushion layer. How to determine the size of the lime-stabilised soil cushion layer to ensure the safety of transmission towers has become an urgent problem to be solved in construction.

5.2. Constitutive Model. The E–v model is an incremental elastic model based on the hyperbolic stress–strain relationship of the soil, which is currently widely used. It is also known as the Duncan–Chang model, and Equation (3) shows that it has eight parameters. The model can reflect the nonlinearity of soil deformation and the influence of stress levels but cannot consider the effects of changes in soil moisture content.

$$E_t = K \cdot p_a \cdot \left(\frac{\sigma_3}{p_a}\right) n \left[\frac{R_f(\sigma_1 - \sigma_3)(1 - \sin \varphi)}{2c \cos \varphi + 2\sigma_3 \sin \varphi}\right]^2$$
$$v_t = \frac{-d\varepsilon_3}{d\varepsilon_1} = \frac{(1 - D\varepsilon_1)f + D\varepsilon_1 f}{(1 - D\varepsilon_1)^2} = \frac{v_i}{(1 - D\varepsilon_1)^2}, \quad (3)$$

where p_a is the standard atmospheric pressure; $p_a = 101.4$ kPa; $v_i = f = G - F \log(\sigma^3/p_a)$; and K, n, φ, c, R_f, G, F, and D are material constants.

Table 2 shows the parameters of the Duncan–Chang model under different water contents. Parameters R_f, F, and D do not change considerably with water content, whereas the other parameters show certain regularity. The variation trends of each parameter with saturation are shown in Figures 9 and 10. By introducing the variable of saturation on the basis of the E–v model, this article enables the model to consider the effect of moisture content changes in engineering.
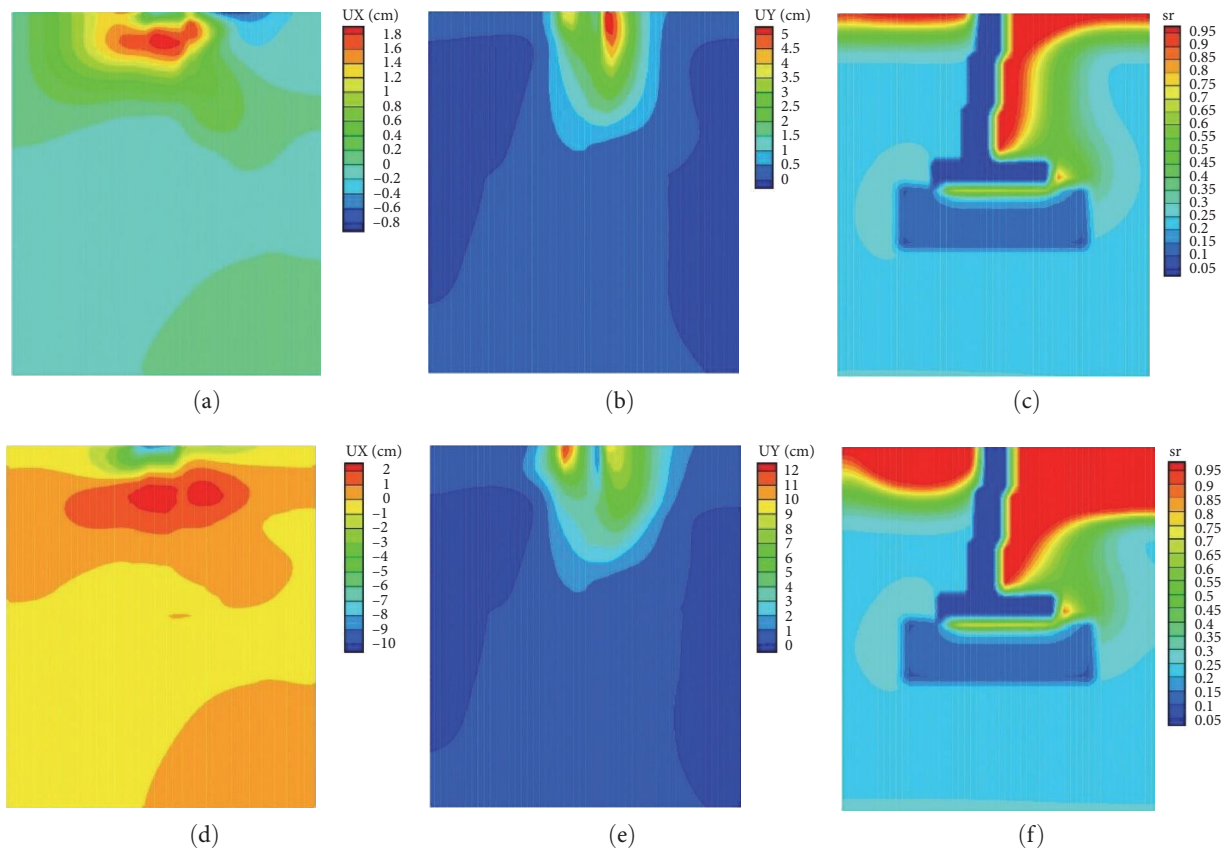
FIGURE 14: Scheme 2: (a)–(c) horizontal displacement, vertical displacement, and saturation after 30 hr of rainfall infiltration; (d)–(f) the horizontal displacement, vertical displacement, and saturation after rainfall infiltration ceases.

5.3. Calculation Scheme. According to the actual form of the transmission tower in engineering, transmission towers can be classified into corner and straight transmission towers. It can be divided into four schemes based on the treatment of the foundation and the measures taken to prevent seepage. The infiltration intensity is shown in Figure 11. In the calculation process, the displacement was interpolated using the quadrilateral eight-node isoparametric element, whereas the seepage was calculated using the quadrilateral four-node isoparametric element. The calculation model and grid division are shown in Figure 12, with a total of 4,200 elements, a vertical height of 20 cm, and a horizontal length of 20 cm. Four types of finite element calculation model are established for different foundation treatment schemes. Load and water infiltration conditions are applied according to the actual situation to make the numerical simulation as practical as possible. To obtain an initial stress field before infiltration that matches the actual situation, each scheme was divided into the following three calculation stages:

(1) During the construction of the transmission tower, the stress and deformation of the foundation and the surrounding soil were calculated by applying 10 steps of load on the concrete tower foundation. The concrete foundation was modelled using a linear elastic model, whereas the surrounding soil was modelled using an *E–v* model.

(2) During a 30 hr rainfall, all the rainfall in the infiltration zone of the transmission tower could be absorbed into the ground.

(3) During a 48 hr rainfall, the infiltration zone of the power transmission tower gradually filled up and water started to flow out. In this scenario, assuming a water head of 3 cm in the infiltration zone, the right side of the equation should be set to a water head of 3 cm. (In practical engineering, the water head in the infiltration area varies with rainfall duration, rainfall amount, and drainage conditions. In this study, the selection of a 3 cm water head was based on the investigation of the most unfavourable conditions.)

For the hydraulic boundary during the rainfall stage, at the initial stage of rainfall, there exist many pores in the soil with strong water absorption capacity, and the infiltration volume is close to the rainfall volume; this boundary condition is called the flow rate boundary. As the rainfall duration increases, the soil moisture near the surface gradually rises and approaches saturation. Subsequent rainfall cannot fully infiltrate into the soil, and surface runoff occurs. Therefore, assuming that suction on the ground approaches zero after 30 hr of rainfall and the ground is covered by rainwater, the boundary condition is changed from a flow rate boundary to a water head boundary.
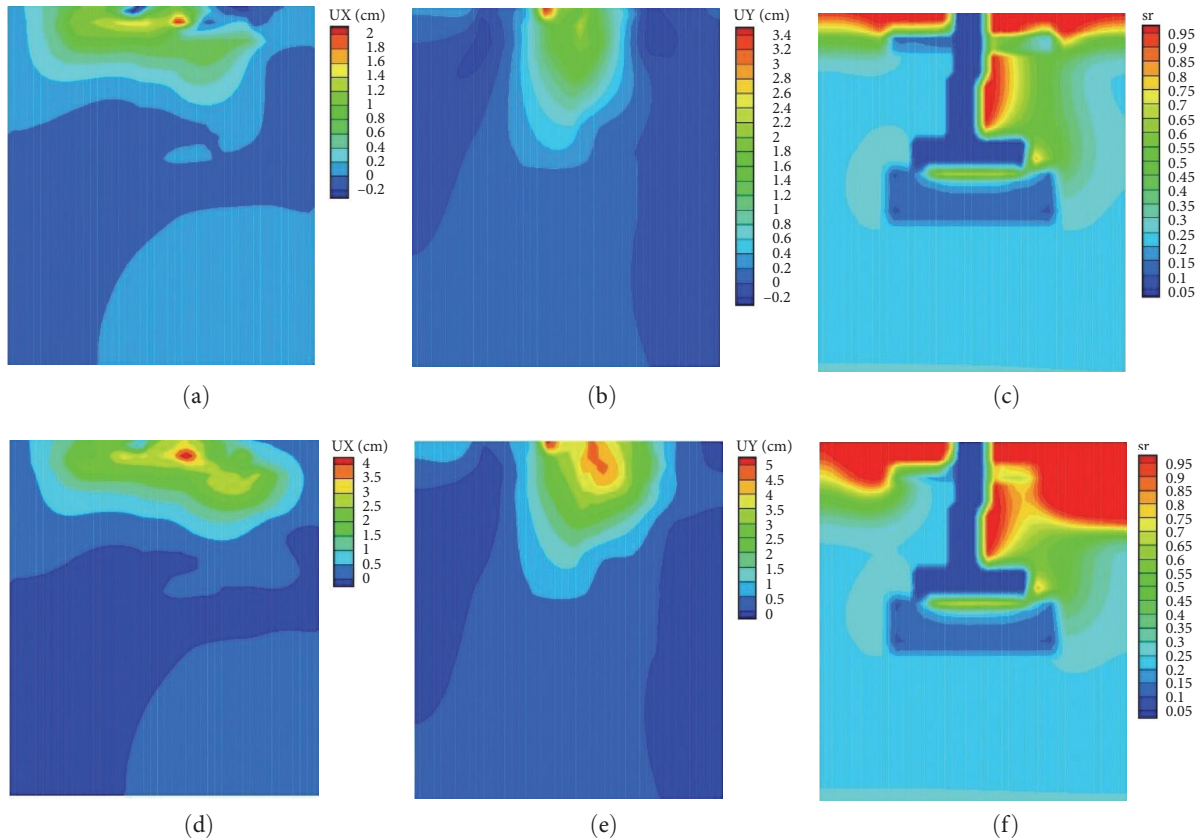
FIGURE 15: Scheme 3: (a)–(c) horizontal displacement, vertical displacement, and saturation after 30 hr of rainfall infiltration; (d)–(f) the horizontal displacement, vertical displacement, and saturation after rainfall infiltration ceases.

5.4. Numerical Simulation. Figures 13–16 show displacement and saturation distribution fields at different stages for four calculation schemes; and Table 3 summarises the horizontal, vertical, and saturation data for the different schemes. The analysis shows that whether it is a straight or sloping foundation, without the use of antiseepage layer or lime-stabilised soil cushion layer treatment, the foundation will experience significant settlement under rainfall infiltration, which may lead to instability of the transmission tower.

The maximum settlement at the top of the tower foundation after 30 hr of rainfall for the four schemes is 6, 5, 3.4, and 11 cm. The maximum settlement at the bottom of the tower foundation for the four schemes is 0.5, 0.8, 0.3, and 8 cm. After 48 hr of rainfall, the maximum settlement at the top of the tower foundation for the four schemes is 6, 12, 5, and 24 cm; whereas the maximum settlement at the bottom of the tower foundation is 0.8, 2, 0.6, and 18 cm. Schemes 1–3 can meet the design requirements. From an economic perspective, Scheme 1 has a significantly larger foundation size compared with Scheme 2 or 3, and the construction difficulty for Scheme 3 is greater than for Scheme 2. In view of tower foundation deformation, inclination, construction, and economic factors, using Scheme 2 is recommended.

Figure 16 shows that for straight foundations treated with a waterproof layer, the tower foundation will still experience significant settlement due to horizontal load, causing cracks between the foundation and waterproof layer.

6. Scheme Optimisation

In the previous section, Scheme 2 has the highest vertical stress; to achieve maximum economic benefit while meeting design requirements, it needed to be optimised. During optimisation, the foundation form, load, and infiltration method were kept constant, and only the thickness of the lime-stabilised soil cushion layer was changed. In Scheme 2, the thickness of the lime-stabilised soil cushion layer was 2,000 mm, whereas Optimised Schemes 1–3 used thicknesses of 1,000, 1,600, and 2,400 mm, respectively.

Figures 17–19 show that as the thickness of the lime-stabilised soil cushion layer increases, the settlement at the midpoint of the foundation bottom decreases, which is generally consistent with the trend. In Optimised Scheme 1, the cushion layer thickness was 1,000 mm, and the midpoint settlement of the foundation was 2.5 cm, which was 0.5 cm higher than the Original Scheme 2. For Scheme 2, the cushion layer thickness was 1,600 mm, and the midpoint settlement of the foundation was 2.3 cm, an increase of 0.3 cm compared with the Original Scheme 2. In Optimised Scheme 2, the cushion layer thickness was 2,400 mm, and the midpoint settlement of the foundation was 1.4 cm, a decrease of 0.6 cm compared with the Original Scheme 2. Thus, Optimised scheme 2 yields the best results.

The curve relationship between the midpoint settlement at the bottom of the foundation and the cushion layer
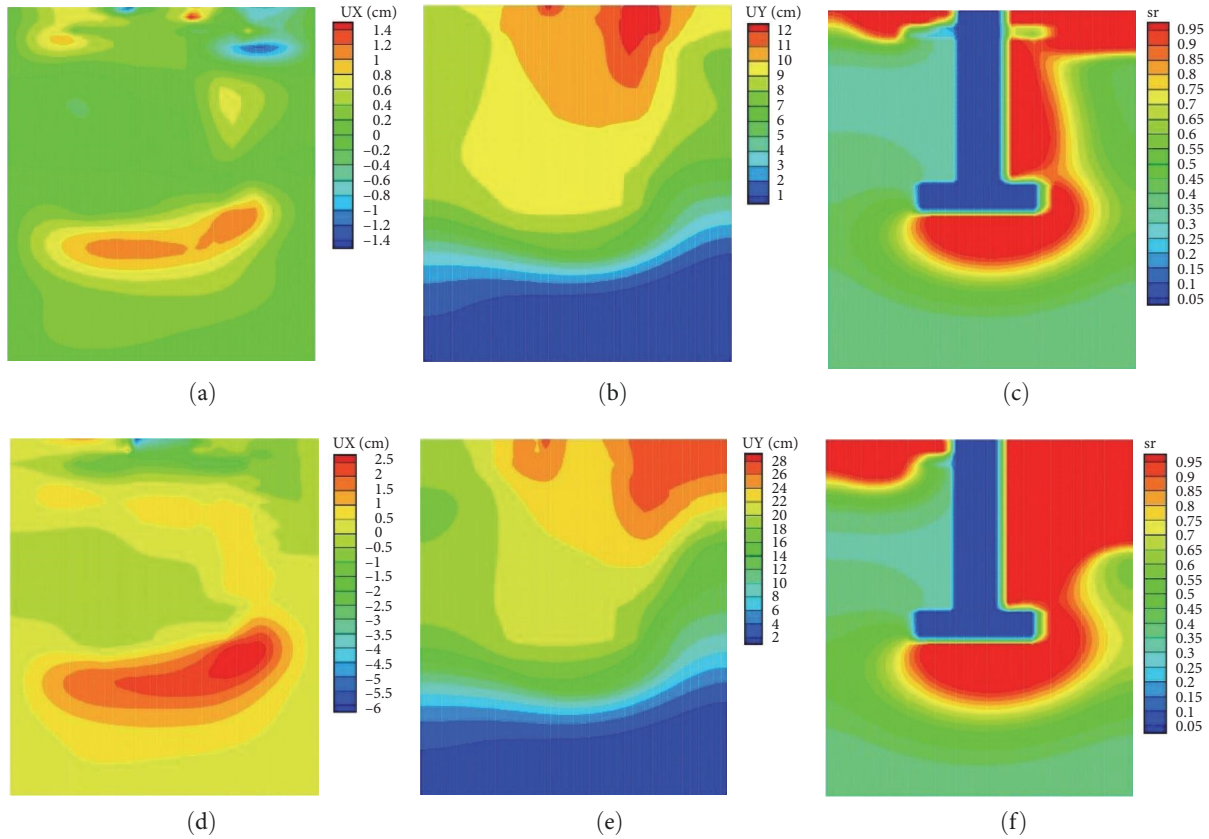
FIGURE 16: Scheme 4: (a)–(c) horizontal displacement, vertical displacement, and saturation after 30 hr of rainfall infiltration; (d)–(f) the horizontal displacement, vertical displacement, and saturation after rainfall infiltration ceases.

thickness was established by comparing the optimised and original schemes (see Figure 20). When the cushion layer thickness is determined, the midpoint wet settlement at the bottom of the foundation can be directly obtained from the graph.

This section optimised the treatment scheme for the inclined footing foundation actually used in the project. By adding a cushion layer with a thickness of 1,600 mm in the demonstration electricity transmission line project in Guanting–Lanzhou East, the design requirements can be meet. If the construction is conducted according to the Original Scheme 2, it will require 77 m³ of lime-stabilised soil to be processed for one tower foundation. Using the optimised scheme would require only 62 m³ of lime-stabilised soil, reducing the amount of lime-stabilised soil required by about 20% compared with the original treatment scheme.

7. Conclusions

Taking the 750 kV demonstration electricity transmission line project in Guanting–Lanzhou East as an example, this article selected typical samples and conducted compression and collapse tests. According to the extensive use of excavated foundation with expanded bottom and inclined footing foundation in the engineering field, multiple treatments for collapsible loess were designed and analysed using finite element analysis to simulate the rainfall infiltration process in the site. The following conclusions were drawn:

(1) Undisturbed loess has a certain structural strength. When the stress exceeds structural strength, loess deformation increases rapidly. The structural strength of loess decreases with the increase in water content. The relationship between saturation and compression modulus can be described using an exponential function.

(2) The loess settlement process can be summarised into four stages: additional compression deformation stage at the beginning of the experiment, collapsing initiation stage as the soil sample gets soaked, collapsing development stage during the saturation period, and collapsing attenuation stage with smooth settlement. These stages correspond to the destruction and recombination process of the structure and have a close relationship with its microstructure evolution.

(3) The analysis of the foundation displacement field and loess saturation field over time after rainfall infiltration shows that the scheme of adding a lime-stabilised soil cushion layer and waterproof layer to the inclined footing foundation used in the project is the most effective. For the scheme of adding a waterproof layer to the excavated foundation with expanded bottom, the foundation will shift under horizontal forces, causing cracks between the foundation and waterproof layer, leading to rainfall infiltration and settlement.

TABLE 3: Statistical table of simulation results.

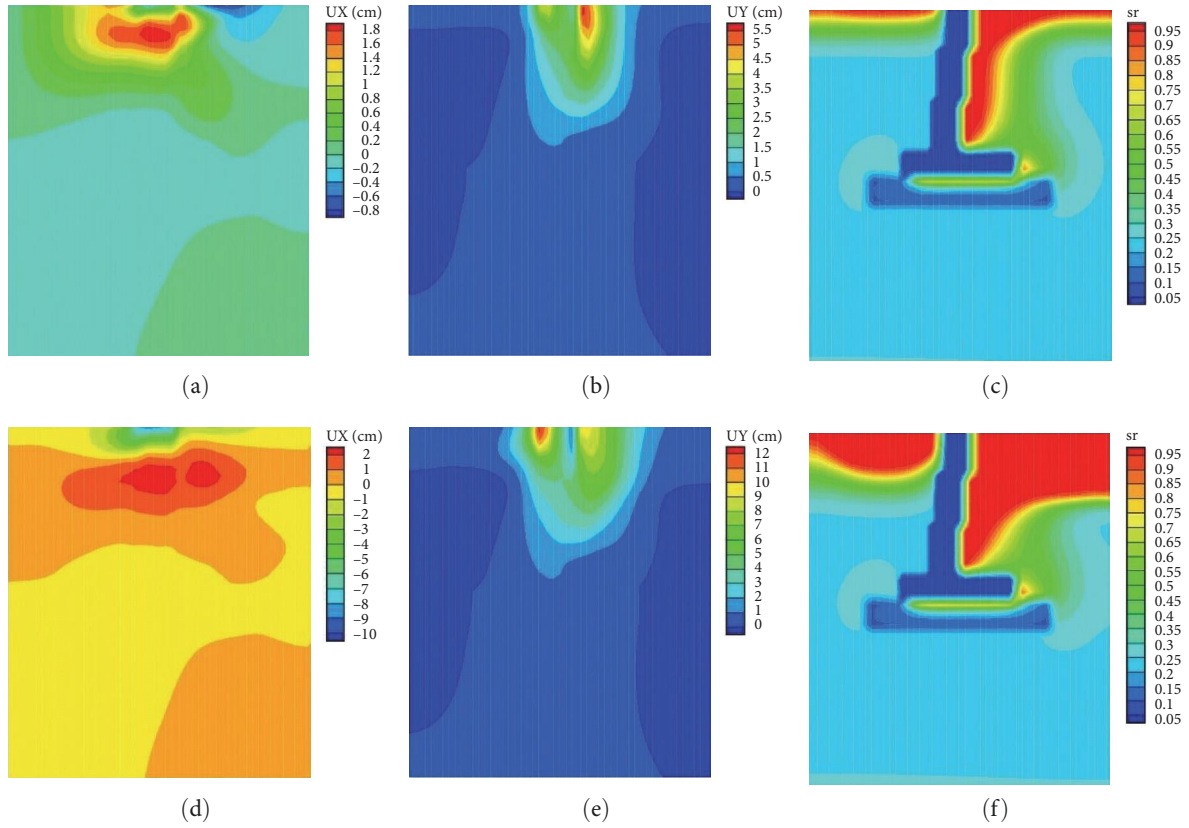| Calculation scheme | Rainfall stage | Deformation at the top of the foundation | | | | Deformation at the bottom of the foundation | | | | | |
		Left		Right		Left		Right		Settlement at the midpoint (cm)	Inclination rate of the foundation
		Vertical (cm)	Horizontal (cm)	Vertical (cm)	Horizontal (cm)	Vertical (cm)	Horizontal (cm)	Vertical (cm)	Horizontal (cm)		
1	Rainfall (30 hr)	3	6	2	4.5	0.5	0.25	0.5	0.25	0.5	0
	End of rainfall (48 hr)	4	6	3	5	0.8	0.5	0.6	0.5	0.7	0.0003
2	Rainfall (30 hr)	4	1.4	5	0.8	0.8	0.1	0.8	0.1	0.8	0
	End of rainfall (48 hr)	12	8	10	4	2	0.3	2	0.3	2	0
3	Rainfall (30 hr)	3.4	0.2	2	0.8	0.3	0.1	0.3	0.1	0.3	0
	End of rainfall (48 hr)	5	2	4.2	3	0.6	0.5	0.6	0.5	0.6	0
4	Rainfall (30 hr)	10	0.2	11	1	9	1	8	1.2	8.5	0.0015
	End of rainfall (48 hr)	24	5	24	2.5	20	2	18	0.3	19	0.003

FIGURE 17: Optimised scheme 1: (a)–(c) horizontal displacement, vertical displacement, and saturation after 30 hr of rainfall infiltration; (d)–(f) the horizontal displacement, vertical displacement, and saturation after rainfall infiltration ceases.
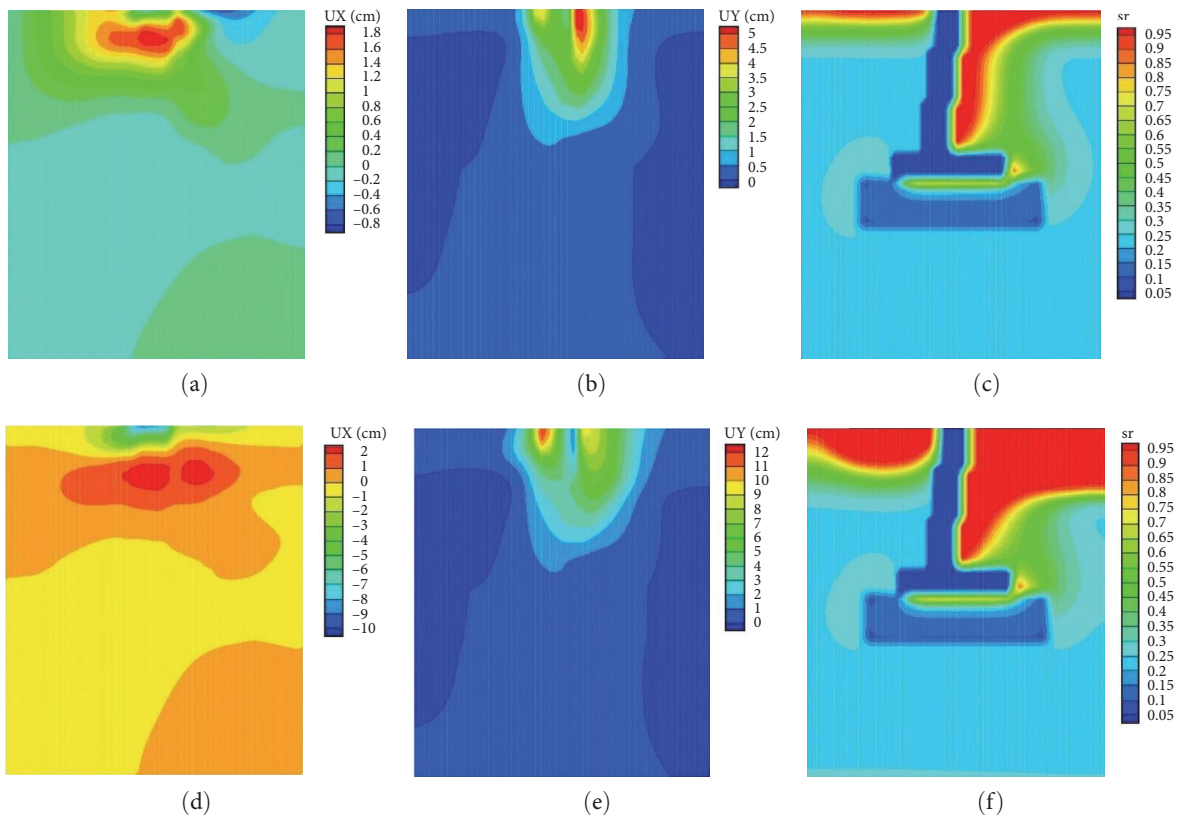

FIGURE 18: Optimised scheme 2: (a)–(c) horizontal displacement, vertical displacement, and saturation after 30 hr of rainfall infiltration; (d)–(f) the horizontal displacement, vertical displacement, and saturation after rainfall infiltration ceases.
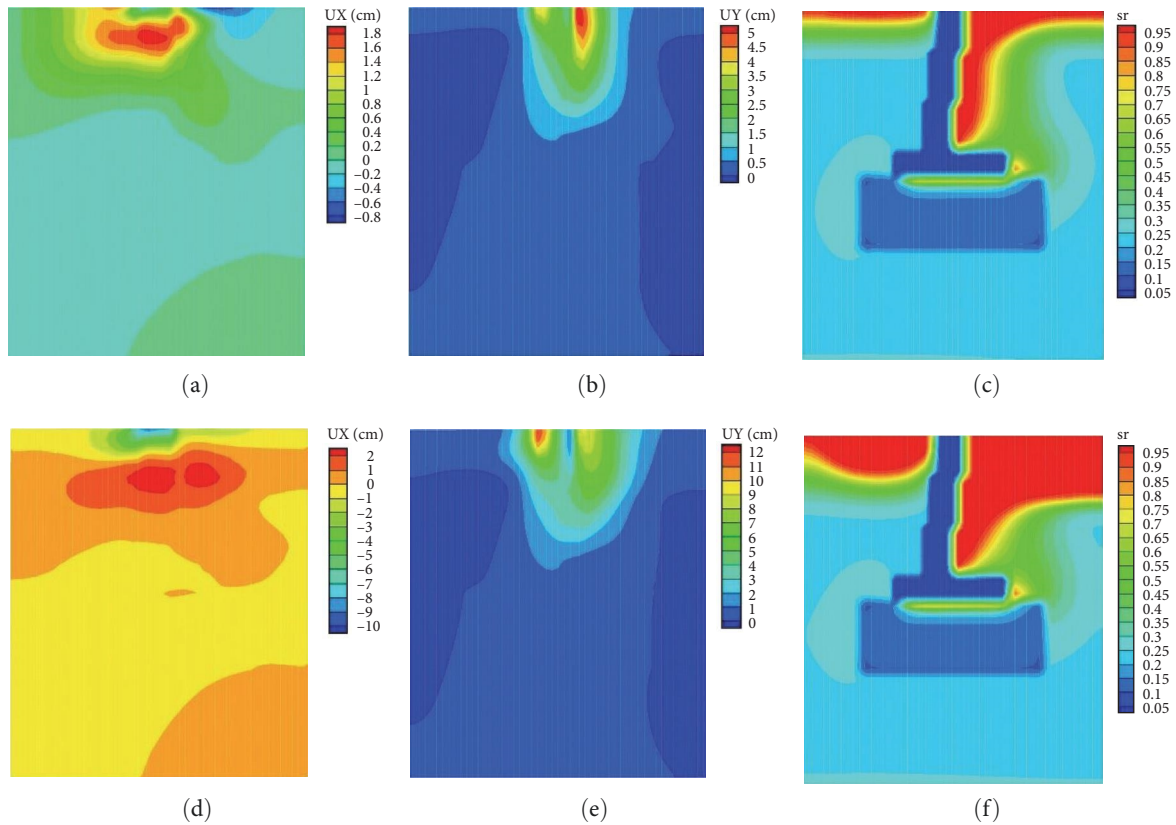
FIGURE 19: Optimised scheme 3: (a)–(c) horizontal displacement, vertical displacement, and saturation after 30 hr of rainfall infiltration; (d)–(f) the horizontal displacement, vertical displacement, and saturation after rainfall infiltration ceases.
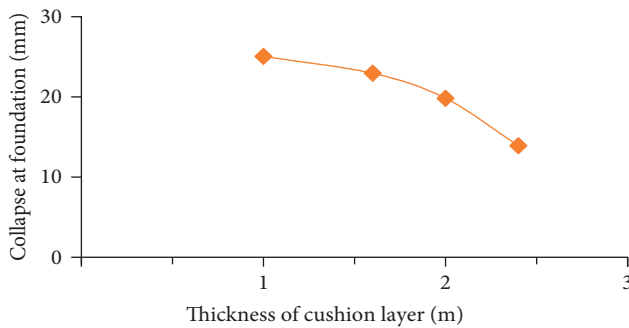

FIGURE 20: Relationship curve between collapsibility and thickness of the cushion layer.

(4) Numerical analysis of the original treatment scheme of adding a waterproof layer to the inclined footing foundation shows that some room still exists for optimisation while satisfying the regulatory requirements. Given that the design scheme needs to balance safety and economy, the thickness of the cushion layer was optimised in this article. The final optimised result shows that a 1,600 mm lime-stabilised soil cushion layer can meet the design requirements while maintaining the same treatment range as before.

(5) The experiment and research were conducted on the actual soil samples and foundation treatment schemes used in the project, combined with a survey of the operation of the transmission lines, proving that the lime-stabilised soil treatment technology used in the northwest region for many years is safe and reliable.

Data Availability

The data supporting the current study are available from thecorresponding author upon request.

Conflicts of Interest

The authors declare that they have no conflicts of interest.

Acknowledgments

References

[1] Y. Li, W. Shi, A. Aydin, M. A. Beroya-Eitner, and G. Gao, "Loess genesis and worldwide distribution," *Earth-Science Reviews*, vol. 201, Article ID 102947, 2020.

[2] Y. Li and Y. Song, "Discussion of the paper "Loess genesis and worldwide distribution" by Yanrong Li, Wenhui Shi, Adnan

Aydin, et al." *Earth-Science Reviews*, vol. 221, Article ID 103151, 2021.

[3] Y. Wang, T. Li, C. Zhao, X. Hou, P. Li, and Y. Zhang, "A study on the effect of pore and particle distributions on the soil water characteristic curve of compacted loess soil," *Environmental Earth Sciences*, vol. 80, Article ID 764, 2021.

[4] B. Zhi, X. Wang, P. Wei et al., "A new method for reducing collapsibility of loess foundation with thicker deposit: the borehole preimmersion method," *Advances in Civil Engineering*, vol. 2021, Article ID 6636347, 15 pages, 2021.

[5] C. Zhu, S. Wang, Z. Ma, X. Dong, and M. Zhang, "Model investigation of anti-seepage measures for the foundation of a heritage building based on soil improvement," *International Journal of Architectural Heritage*, vol. 16, no. 9, pp. 1414–1431, 2022.

[6] T. Eskisar, "The role of carbide lime and fly ash blends on the geotechnical properties of clay soils," *Bulletin of Engineering Geology and the Environment*, vol. 80, pp. 6343–6357, 2021.

[7] Y. Zheng, C. Li, and Q. Ma, "Feasibility of lime-modified carbonate soil for highway subgrade filling," *Asia-Pacific Journal of Chemical Engineering*, vol. 15, no. S1, Article ID 12463, 2020.

[8] M. Ismeik and F. Shaqour, "Effectiveness of lime in stabilising subgrade soils subjected to freeze–thaw cycles," *Road Materials and Pavement Design*, vol. 21, no. 1, pp. 42–60, 2020.

[9] J.-J. Gao, H. Xu, J.-W. Qian, Y.-F. Gong, L.-T. Zhan, and P. Chen, "Settlement behavior of soft subgrade reinforced by geogrid-encased stone column and geocell-embedded sand cushion: a numerical analysis," *Advances in Civil Engineering*, vol. 2020, Article ID 8874520, 11 pages, 2020.

[10] Y. Zhang, L. Xie, B. He, and P. Zhao, "Research on the impact force of rockfall impacting sand cushions with different shapes," *Applied Sciences*, vol. 12, no. 7, Article ID 3540, 2022.

[11] Y. Mei, S. Zhang, C. Hu et al., "Field test study on dynamic compaction in treatment of a deep collapsible loess foundation," *Bulletin of Engineering Geology and the Environment*, vol. 80, pp. 8059–8073, 2021.

[12] C. Zhou, H. Jiang, Z. Yao et al., "Evaluation of dynamic compaction to improve saturated foundation based on the fluid–solid coupled method with soil cap model," *Computers and Geotechnics*, vol. 125, Article ID 103686, 2020.

[13] D. Abdizadeh, M. S. Pakbaz, and B. Nadi, "Model test study for dynamic compaction in slope on the bearing capacity of the strip footing," *KSCE Journal of Civil Engineering*, vol. 25, pp. 1700–1704, 2021.

[14] S. He, X. Wang, H. Fan, H. Wang, R. Ren, and C. Guo, "The study on loess liquefaction in China: a systematic review," *Natural Hazards*, vol. 103, pp. 1639–1669, 2020.

[15] M. Węgiel and T. Rakowski, "Circulating biomarkers as predictors of left ventricular remodeling after myocardial infarction," *Advances in Interventional Cardiology*, vol. 17, no. 1, pp. 21–32, 2021.

[16] F. Zhang, J. Dong, X. Yang, B. Lian, and X. Wang, "Study on the hydro-thermal-mechanical characteristics of the lime-soil compaction pile in the forming process," *Advances in Materials Science and Engineering*, vol. 2021, Article ID 7701423, 9 pages, 2021.

[17] C. Zhu, X. Zhou, and S. Wang, "Foundation treatment assessment and postconstruction settlement prediction of a loess high fill embankment: a case study," *Shock and Vibration*, vol. 2020, Article ID 8864690, 22 pages, 2020.

[18] C. Gao, G. Du, S. Liu, D. Zhang, K. Zhang, and B. Zeng, "Field study on the treatment of collapsible loess using vibratory probe compaction method," *Engineering Geology*, vol. 274, Article ID 105715, 2020.

[19] C. Gao, G. Du, S. Liu, H. He, and D. Zhang, "The microscopic mechanisms of treating collapsible loess with vibratory probe compaction method," *Transportation Geotechnics*, vol. 27, Article ID 100492, 2021.

[20] C. Zhu and N. Li, "Ranking of influence factors and control technologies for the post-construction settlement of loess high-filling embankments," *Computers and Geotechnics*, vol. 118, Article ID 103320, 2020.

[21] Z. Zhu, Y. Zhou, K. Han, H. Wu, and S. Zhao, "Liquefaction and reliquefaction characteristics of aeolian sand foundation reinforced by precast cement piles based on shaking table test," *Geofluids*, vol. 2022, Article ID 5344230, 13 pages, 2022.

[22] S. Farhangdoust, A. Mehrabi, and S. Nolan, "GFRP composite bars for splicing prestressed precast concrete piles: design and experimental investigation," *Engineering Structures*, vol. 272, Article ID 114969, 2022.

[23] Y. Li, S. Xu, H. Liu, E. Ma, and L. Wang, "Displacement and stress characteristics of tunnel foundation in collapsible loess ground reinforced by jet grouting columns," *Advances in Civil Engineering*, vol. 2018, Article ID 2352174, 16 pages, 2018.

[24] K. N. Flynn and B. A. McCabe, "Applicability of CPT capacity prediction methods to driven cast-in-situ piles in granular soil," *Journal of Geotechnical and Geoenvironmental Engineering*, vol. 147, no. 2, 2021.

[25] M. Zhou, Z. Li, Y. Han, P. Ni, and Y. Wang, "Experimental study on the vertical bearing capacity of stiffened deep cement mixing piles," *International Journal of Geomechanics*, vol. 22, no. 5, 2022.

[26] C. Phutthananon, P. Jongpradist, D. Dias, X. Guo, P. Jamsawang, and J. Baroth, "Reliability-based settlement analysis of embankments over soft soils reinforced with T-shaped deep cement mixing piles," *Frontiers of Structural and Civil Engineering*, vol. 16, pp. 638–656, 2022.

[27] P. Voottipruex, D. T. Bergado, T. Suksawat, P. Jamsawang, and W. Cheang, "Behavior and simulation of deep cement mixing (DCM) and stiffened deep cement mixing (SDCM) piles under full scale loading," *Soils and Foundations*, vol. 51, no. 2, pp. 307–320, 2011.

[28] Z. Liu, Q. Lu, J. Qiao, and W. Fan, "In situ water immersion research on the formation mechanism of collapsible earth fissures," *Engineering Geology*, vol. 280, Article ID 105936, 2021.

[29] S. H. Jafari, S. H. Lajevardi, and M. Sharifipour, "Correlation between small-strain dynamic properties and unconfined compressive strength of lime-stabilized soft clay," *Soil Mechanics and Foundation Engineering*, vol. 59, pp. 331–337, 2022.

[30] P. Li, S. Vanapalli, and T. Li, "Review of collapse triggering mechanism of collapsible soils due to wetting," *Journal of Rock Mechanics and Geotechnical Engineering*, vol. 8, no. 2, pp. 256–274, 2016.

[31] L. Zhang, F. N. Dang, X. Wang, J. L. Ding, J. Gao, and Y. Zhang, "Estimation of earth pressure against retaining walls with different limited displacement modes based on elastic theory," *Journal of Mountain Science*, vol. 19, pp. 289–304, 2022.

[32] I. Y. Dezhina, "Deformation analysis of loess foundation beds with allowance for elastoplastic properties of the soil," *Soil Mechanics and Foundation Engineering*, vol. 42, pp. 9–14, 2005.

[33] C. Zhou and C. W. W. Ng, "A new thermo-mechanical model for structured soil," *Géotechnique*, vol. 68, no. 12, pp. 1109–1115, 2018.

[34] J. Lei, Z. Zhou, D. Han et al., "Centrifuge model tests and settlement calculation of belled and multi-belled piles in loess area," *Soil Dynamics and Earthquake Engineering*, vol. 161, Article ID 107425, 2022.

[35] S.-L. Jin, J. Yan, L.-C. Li, B. Wang, S.-F. Wu, and L.-M. Sun, "New method for the mechanical characteristics of self-weight collapsibility testing of loess foundation based on centrifugal model test," *Mechanics of Advanced Materials and Structures*, pp. 1–10, 2022.

[36] P. An, A. Zhang, Y. Xing, B. Zhang, W. Ni, and W. Ren, "Experimental study on settling characteristics of thick self-weight collapsible loess in Xinjiang Ili region in China using field immersion test," *Soils and Foundations*, vol. 58, no. 6, pp. 1476–1491, 2018.

[37] Y. Xu, C. F. Leung, J. Yu, and W. Chen, "Numerical modelling of hydro-mechanical behaviour of ground settlement due to rising water table in loess," *Natural Hazards*, vol. 94, pp. 241–260, 2018.

[38] Y. Liu and H. Lai, "Load characteristics of tunnel lining in flooded loess strata considering loess structure," *Advances in Civil Engineering*, vol. 2019, Article ID 3731965, 13 pages, 2019.

[39] G. Guorui, "Classification of microstructures of loess in China and their collapsibility," *Scientia Sinica*, vol. 24, no. 7, pp. 962–974, 1981.

[40] X. Zhang, Y. Lu, X. Li, Y. Lu, J. Sun, and W. Pan, "Multilevel collapsibility of loess under irrigation in Jinya Town, Gansu Province, China," *Advances in Civil Engineering*, vol. 2019, Article ID 2153679, 13 pages, 2019.

[41] L. Deng, W. Fan, S. Liu, Y. Chang, Y. Dai, and Y. Li, "Quantitative research and characterization of the loess microstructure in the Bai Lu Tableland, Shaanxi Province, China," *Advances in Civil Engineering*, vol. 2020, Article ID 3681382, 14 pages, 2020.